Accurate Technique for Measuring Electrical Permittivity of Biological Tissues at Low Frequencies and Sensitivity Analysis

3 authors, including:

Seyyed Hesabgar
University of Ottawa

Abbas Samani
The University of Western Ontario

Some of the authors of this publication are also working on these related projects:

Project   Breast Cancer View project

Project   Image based COPD GOLD stage assessment View project

Accurate Technique for Electrical Permittivity Measurement of Biological Tissue Specimens at Low Frequencies and Sensitivity Analysis

Seyyed M. Hesabgar, Reza Jafari , *Member, IEEE*, Abbas Samani

Abstract—This paper presents an accurate technique for measuring electrical permittivity (EP) of small biological tissue specimens at low frequencies while measurement sensitivity to specimen geometry and tissue specimen inhomogeneity is investigated. Accurate EP measurement of various biological tissues, including healthy and pathological tissues, can pave the way for a wide range of medical applications such as electrical impedance imaging. This novel technique utilizes a high precision hardware for impedance measurement of a capacitive structure formed by two conductive plates and the tissue specimen as its dielectric. The capacitance part of the measured impedance is processed using an inverse finite element framework to determine the tissue electrical permittivity. This framework considers specimen's accurate geometry and boundary conditions. After successful validation, the technique was employed to measure electrical permittivity of several specimens of bovine heart, liver and bone tissues. The proposed technique is reliable and is expected to offer improved measurement accuracy and repeatability of electrical permittivity of homogeneous or multi-layered tissue specimens, especially at low frequencies.

Keywords—biological tissue, electrical permittivity, measurement, low frequency, boundary element, finite element, inverse problem

I. INTRODUCTION

Accurate measurement of electrical permittivity (EP) of biological tissue is important for a broad range of applications, including development of medical imaging techniques that map tissue electrical properties [1-3] and studying biological tissue interaction with electromagnetic fields [4]. Among other applications, EP imaging has a good potential as a diagnostic tool. EP properties of biological tissues cover a broad range, which implies that EP imaging may produce high contrast images with enhanced diagnostic data [5-10]. In this application, EP can be potentially used as a biomarker to differentiate between various pathologies and to detect and classify tissue abnormalities such as tumors [2,6,11]. Thus, accurate EP measurement of various biological tissues can pave the way for many medical applications, including effective interpretation of electric capacitance images for disease diagnosis. Studies have shown that, with higher frequencies, relative permittivity (ε_r) decreases significantly while electrical conductivity (σ) increases [7,8]. This implies that EP imaging at low frequencies is highly advantageous as it can provide images with broad dynamic range and high contrast. Furthermore, energy loss in biological tissue at low frequencies is significantly lower than at high frequencies due to the lower conductance, rendering tissue electrical property imaging safer. While significant efforts have been dedicated to study tissue EP at high frequencies, less efforts have been made to its study at low frequencies [9].

Peyman et al. [11] measured ε_r of various porcine tissues (e.g. gray matter and spinal cord) at high frequencies ranging from 50 MHz to 20 GHz. They consistently confirmed that ε_r increases with lower frequencies. To investigate tissue EP variations during embryo development Peyman et al. [12] and Lu et al. [13] measured EP of human and rat fetal tissues at different ages at frequencies of 100 kHz to 20 kHz. Their results showed a general trend of EP reduction with age. Furthermore, Meaney et al. [5] also showed a strong correlation between both EP and electrical conductivity with bone volume fraction. Among researchers who measured EP of pathological tissues, Joines et al. [14] measured EP of various malignant tumors acquired from rats and humans. Their measurement was conducted at frequencies of 30 MHz to 2 GHz where they showed that EP of malignant tissues are up to 233% greater than their normal tissue counterparts. For EP assessment of breast and prostate benign and malignant tumors, Halter et al. [2] showed that tissue EP can be used to differentiate between malignant and benign tumors and to assess cancer grade.

More recently, Hesabgar et al. measured dielectric properties of malignant breast tissue in xenograft mice. Their results show that EP of the breast tumor is more than an order of magnitude higher than that of normal tissue [20]. To our knowledge, EP measurement methods of ex-vivo tissue developed over the past three decades have used conventional measurement techniques by utilizing open-end coaxial cable in conjunction with analytical model based on a lumped parameter approach. More recently, such measurement systems also utilized vector network analyzer (VNA). In these techniques the reflection coefficient or admittance of the probe–sample interface is measured and used to approximate the specimen's EP [6]. Issues with the open-ended coaxial probe methods that may dramatically distort the desired measurements are a) air gap irrespective of its size, b) in heterogeneous samples, the penetration depth is a function of probe diameter, c) effective penetration depth of electric field in tissue samples is limited, and d) accuracy achieved in this measurement approach is dependent on the reflected signal and reflection coefficient at the probe–sample interface [6].

At low frequencies (below MHz range), measurement errors lead to very high amplification of the tissue EP estimation errors. As shown in this article, the limited electric field penetration depth may lead to large errors when the tissue sample has even small amount of inhomogeneity, confirming the importance of accounting for tissue actual geometry and boundary conditions. The latter can be effectively achieved through a distributed parameter modeling approach formulated using a finite element (FE) or a boundary element (BE) framework. Among researchers who pointed out limitations of current conventional EP measurement techniques, Gabriel and Peyman [10] and Jarvis et al. [15,16]. They demonstrated that the percentage error of using the conventional approach at low frequencies can exceed 50%. As such a robust technique for EP measurement of biological tissue, which takes into account specimen's geometry, inhomogeneity and boundary conditions reliably while having low sensitivity to raw data measurement errors at low frequencies, is desirable.

In [24], an accurate technique for measuring electrical permittivity of biological tissues at low frequencies and a measurement sensitivity to tissue inhomogeneity was presented. In this paper, we further expand that work through introducing a novel technique with improved accuracy of EP measurement of small biological tissue specimens. The measurement set up includes a custom-made capacitive sensor with the tissue sample as its dielectric. As such, it does not suffer from EP estimation error amplification at low frequencies. It uses the distributed parameter FE approach for modeling the specimen, including accurate modelling of its geometry and boundary conditions accurately, leading to low sensitivity to tissue inhomogeneity.

II. METHOD

A. Conventional techniques of EP measurement

Conventional techniques use open-end coaxial probes in conjunction with VNAs as shown on Figure 1. As illustrated in this figure, the VNA transmits an electromagnetic incident wave (incident signal) into the coaxial probe which is pressed against the tissue sample at one end and attached to the VNA at the other end. The incident signal ($Vi \angle \beta$) propagates into the probe and hits the sample at the probe-sample interface region where part of it reflects back to the VNA through the probe due to the impedance mismatch. This reflected wave ($Vr \angle \alpha$) affects the amplitude and phase of the incident wave ($Vi \angle \beta$) in the coaxial probe. By measuring and analyzing the phase and amplitude of the incident and reflected waves, the VNA estimates the sample's impedance. These techniques have limitations especially under low frequencies. The following equation, which is based on a lumped parameter approach, shows a fundamental relationship between incident and reflected waves and electrical impedance of the two sides of the probe-sample interface [17].

$$\Gamma = \frac{Vr \angle \alpha}{Vi \angle \beta} = \frac{Z_s - Z_i}{Z_s + Z_i} \qquad (1)$$

This leads to:

$$Z_s = \frac{(1+\Gamma)}{(1-\Gamma)} Z_i = \gamma Z_i \qquad (2)$$

where Γ is the reflection coefficient at the probe-sample interface, Vr and α are the amplitude and phase angle of the reflected wave, Vi and β are the amplitude and phase angle of the incident wave, Z_i is the impedance of the coaxial probe and Z_s is the impedance of the sample.
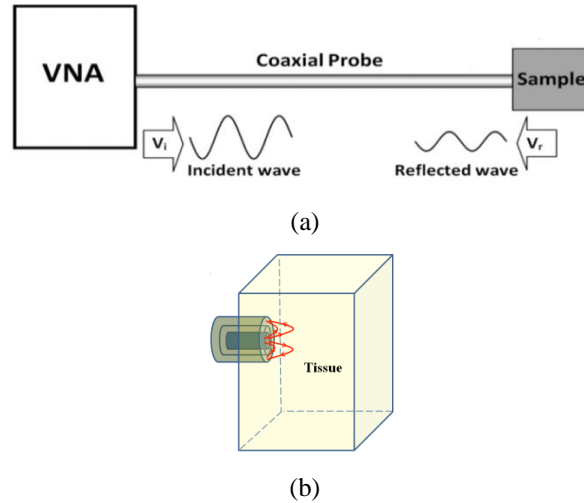

(a)

(b)

Fig. 1. Conventional techniques: a) schematic of the experimental setup based on open-end coaxial probes, and b) model of the end of coaxial probe , the tissue sample and schematic electric field lines.

Based on (1), at low frequencies where the impedance of biological tissues is significantly higher than the impedance of coaxial probe, the reflection coefficient at the probe-sample interface becomes very close to 1, leading to a very large γ value. This implies that, at low frequencies, inevitable raw data measurement errors involved in the conventional EP measurement technique leads to highly magnified error in the sample EP estimation

B. Overview of the proposed technique

The proposed EP measurement technique consists of tissue impedance data acquisition followed by data processing to estimate the tissue's EP. For tissue data acquisition, a freshly excised specimen of the tissue is placed between two plates of a custom-made impedance measurement sensor and, after excitation using low frequency voltage, the resultant resistance (R_m) and capacitance (C_m) values are measured. C_m is a physical property of the capacitor which consists of two conductors and the tissue sample (dielectric) sandwiched between them. It depends on the geometry of conductors and permittivity of the tissue which is an intrinsic tissue property.

B.1 Forward Problem

Assuming that the sample tissue is a linear and isotropic region Ω, the forward problem is governed by the following equation [18]:

$$\nabla\big(\kappa(r)\nabla U(r)\big) = 0 \qquad (3)$$

where $U(r)$ is the electric potential at position $r = (x, y, z)$, and $\kappa(r) = \sigma + j\omega\varepsilon$ is the internal admittivity distribution in the tissue specimen. Here σ and ε are the electrical conductivity and permittivity, respectively, and ω is the angular frequency. Appropriate boundary conditions are applied on the boundaries of the solution domain.

$$\begin{cases} U(r) = 0 & r \in \Gamma_1 \\ U(r) = V_s & r \in \Gamma_2 \\ \kappa(r)\nabla U(r).n(r) = 0 & r \in \Gamma_3 \end{cases} \qquad (4)$$

Applying a current source, Dirichlet boundary conditions on Γ_1, and Neumann boundary condition on Γ_2 and Γ_3 are defined as follows:

$$\begin{cases} U(r) = 0 & r \in \Gamma_1 \\ \kappa(r)\nabla U(r).n(r) = 0 & r \in \Gamma_2 \\ \kappa(r)\nabla U(r).n(r) = j_s & r \in \Gamma_3 \end{cases} \qquad (5)$$

where j_s is the current density related to the current source. The electrical impedance Z across two electrodes is obtained from dividing the voltage $V = \Delta U$ by the current I passing the electrode. Here ΔU is the potential difference between the two electrodes. The current is calculated by current density over the electrode area which is calculated from the distribution of electric field, $\vec{J} = \sigma_c\vec{E}$. Thus, electrical impedance of the sample, $Z = R - jX$, is expressed as follows:

$$Z = \frac{V}{\int_R \vec{j}.d\vec{S}} \qquad (6)$$

where $\vec{S}$ is the normal vector to the electrode/tissue interface. In general, the resistance R is a function of electrical conductivity σ and the reactance X and capacitance C, $X = 1/(\omega C)$ are a function of permittivity ε. The ac equivalent circuit of biopotential electrode in contact with an electrolyte is shown in Fig. 2 [23]. The C_d is the double layer capacitance and R_d represents the leakage resistance across this double layer. R_s is the series resistance related to interface effects and due to resistance in the tissue or electrolyte. Supposing R_s is determined from a high frequency measurement, one can obtain $Z_d = Z - R_s$.
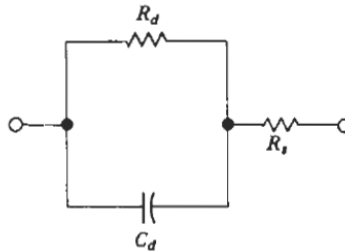

Fig. 2. The ac equvalent circuit of the ac equivalent circuit of biopotential electrode in contact with an electrolyte [23],.

Using the relationship $\mathbf{Z}_d = \frac{1}{\frac{1}{R_d}+j\omega C_d}$, the resistance R_d and the capacitance C_d can be obtained as

$$R_d = |\mathbf{Z}_d|\sqrt{1 + \tan^2(\sphericalangle \mathbf{Z}_d)} \qquad (7)$$

and

$$C_d = \frac{-\tan(\sphericalangle \mathbf{Z}_d)}{\omega |\mathbf{Z}_d|\sqrt{1+\tan^2(\sphericalangle \mathbf{Z}_d)}} \, . \qquad (8)$$

Equations (6)-(8) show that the relationship between the resistance R_d and σ and the capacitance C_d and ε are complex as, in general, E is a function of position. The electric potential and the E field can be calculated by solving (6) which can be achieved numerically using the FE method. Equation 6 also shows that the impedance $\mathbf{Z}$ depends on the geometry of the conductor plates and geometry and permittivity of the materials between them. Although, the estimation of tissue specimen electrical conductivity can be studied in this paper, we focus on the estimation of the electrical permittivity because of the importance of accurate measurement of electrical permittivity in biological tissue.

B.2 Optimization based numerical inversion approach

The inversion part of the proposed inverse algorithm utilizes a constrained optimization algorithm [21] which seeks a relative EP value (ε_r) that leads to the closest match between the capacitance value obtained from FE models (C_c) and its experimentally measured counterpart (C_m). Although the BE method is ideal, at this stage of research, the FE method was used to calculate C_c. For this purpose, an objective cost function representing the absolute difference between experimental and simulated capacitance values was defined. Given that the range of ε_r values for biological tissues is known based on the literature, constrained (bounded) optimization was used to determine it such that the risk of convergence to local minima is minimized. Therefore, the constrained minimization problem is formulated at the k-th iteration as follows:

$$f(\varepsilon_r) = |C_{d.m} - C_{d.cal}(\varepsilon_r)|$$

$$\begin{cases} Min. \quad f(\varepsilon_r) \\ sub.\ to \quad \varepsilon_{rL} \le \varepsilon_{rk} \le \varepsilon_{rU} \end{cases}$$

We used lower bound ε_{rL} values of 100 and 1000 and upper bound ε_{rU} values of 5000 and 50000 for the trabecular bone and soft tissues (heart and liver specimens), respectively. The algorithm is launched with an input ε_r initial guess value. The optimization process is terminated when the objective function value becomes sufficiently small.

As such, the inverse problem was formulated as a 1D optimization problem for homogenous samples, where ε_r is the unknown parameter to be determined. In this optimization problem, the calculation starts with an initial guess value of $\varepsilon_r = \varepsilon_{r0}$. This value is modified iteratively using the optimization algorithm until the difference between the sensor's capacitance value (C_c) calculated using the FE model and its measured counterpart (C_m) is minimum. The last ε_r value will be taken as the specimen's relative permittivity value. Experimental setup for impedance measurement has been explained in [20].
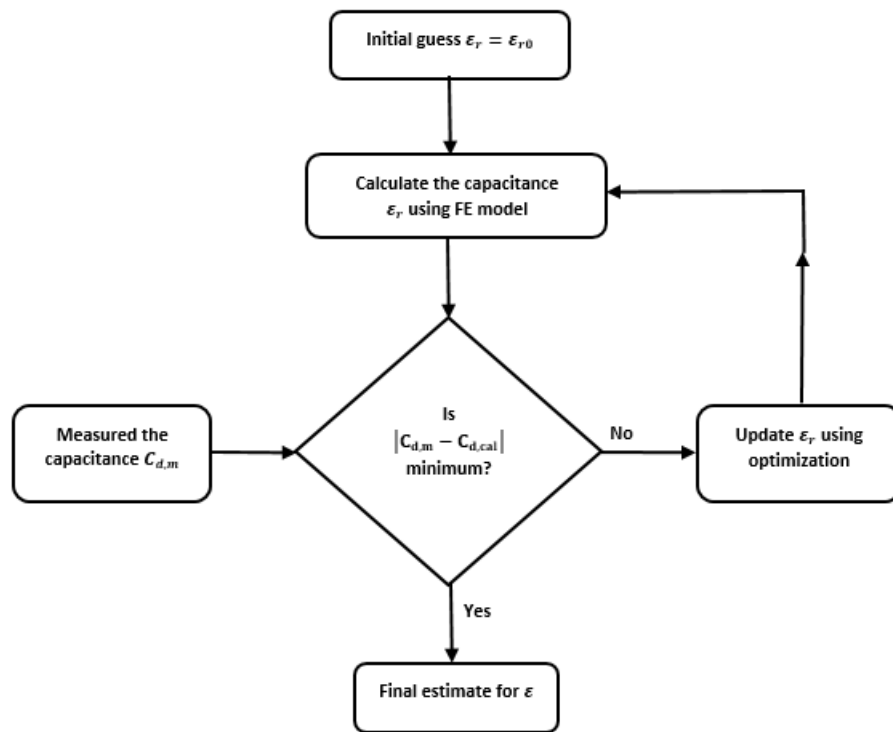
Fig. 3. Flowchart of the inverse problem algorithm: The algorithm is based on a FE or BE forward model and is used to estimate tissue specimen relative electrical permittivity.
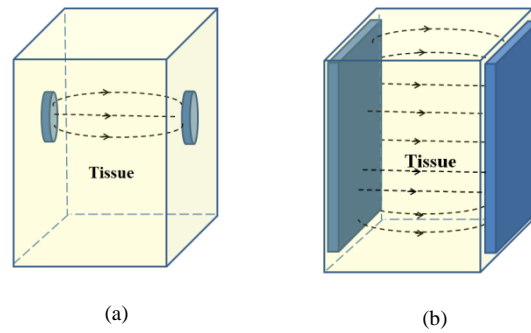

(a)   (b)

Fig. 4. Proposed technique: models of electrodes, tissue samples and schematics pf electric field lines a) disk electrodes and b) plate electrodes.
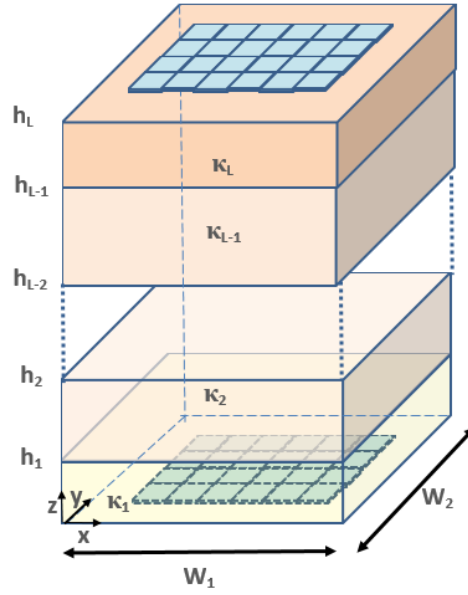
Fig. 5. Proposed technique: models of electrodes, four-layered tissue samples .

III. MULTILAYERED TISSUE SPECIMEN - ANALYTICAL SOLUTION FOR FORWARD PROBLEM

In this section, a problem with multilayer tissue specimen and multielectrode arrays is presented. The analytical solution of this problem was presented in a closed form for the amplitudes of components of Fourier series in the literature [25-29]. However, the problem has been solved with the following considerations a) it includes two or three-layered tissues, b) it is not amenable to to expansion for tissue specimens with more than three layers, and c) the reference potential has not been used in the potential solution. To obtain an analytical solution for more than three layers, a set of algebraic equations approximating the governing differential equations in conjunction with algebraic equations modelling boundary conditions must be solved. The geometry in this problem is modeled as a rectangular parallelepiped with electrodes placed in contact with the top and bottom surfaces of the geometry. This is an approximate model for the tissues placed between the electrode arrays to form a rectangular box with electrode plates. The forward problem is formulated as follows: consider a rectangular region with L layers and the tissue domain is defined to be within $0 \leq x \leq W_1$, $0 \leq y \leq W_2$, $h_0 \leq z \leq h_L$. In each layer the governing equation for the potential is obtained as

$$\nabla^2 \boldsymbol{U}(x,y,z) = 0 \qquad 0 \leq x \leq W_1, 0 \leq y \leq W_2, h_{i-1} \leq z \leq h_i \qquad (10)$$
$$i = 1,2,\dots,L$$

where $\boldsymbol{U}(x,y,z)$ is the phasor of the time function $U(x,y,z,t)$ as $u(x,y,z,t) = Re\{\boldsymbol{U}(x,y,z)e^{j\omega t}\} = |\boldsymbol{U}|\cos(\omega t + \sphericalangle\boldsymbol{U})$.
The Neumann boundary condition on the side surfaces is zero, leading to

$$\frac{dU(x=0,y,z)}{dx} = 0 \quad , \quad \frac{dU(x=W_1,y,z)}{dx} = 0$$
$$\frac{dU(x,y=0,z)}{dy} = 0 \quad , \quad \frac{dU(x,y=W_2,z)}{dy} = 0$$

The current density is applied on the top and bottom surfaces by electrodes. Hence, the Neumann boundary conditions on these surfaces lead to

$$\kappa_L \frac{dU(x,y,h_L)}{dz} = \boldsymbol{j}^t(x,y,h_L) \qquad (12)$$

and

$$-\kappa_1 \frac{dU(x,y,z=h_0)}{dz} = j^b(x,y,h_0) \qquad (13)$$

The current density on electrodes on the top surface are considered as

$$j(x,y,z=h_L) = \begin{cases} \frac{I_e}{A_e} & for\ (x,y)\ on\ the\ electrode\ e\ carring\ current \\ 0 & otherwise \end{cases} \qquad (14)$$

and the current density on electrodes on the bottom surface are considered as

$$j(x,y,z=h_0) = \begin{cases} \frac{-I_e}{A_e} & for\ (x,y)\ on\ the\ electrode\ e\ carring\ current \\ 0 & otherwise \end{cases} \qquad (15)$$

The Dirichlet boundary condition is considered as

$$U(x_0, y_0, z_0 = h_0) = U_0 \qquad (16)$$

The interfacial conditions should be taken into account so that the potential $U(x,y,z)$ and the current density $\kappa \frac{\partial U(x,y,z)}{\partial n}$ has to be continuous across layers. Consequently, for i=1,2,3, and L-1 one can apply the following conditions

$$U_i(x,y,z)\Big|_{z=h_i^-} = U_{i+1}(x,y,z)\Big|_{z=h_i^+} \qquad (17)$$

and

$$\kappa_i \frac{\partial U_i(x,y,z)}{\partial n}\Big|_{z=h_i^-} = \kappa_{i+1} \frac{\partial U_{i+1}(x,y,z)}{\partial n}\Big|_{z=h_i^+}. \qquad (18)$$

The simple method of separation of variables can be used to solve this problem for U_i for $h_{i-1} \le z \le h_i$, which leads to [25]

$$U_i(x,y,z) = A_{i_{0,0}} + B_{i_{0,0}}z + \sum_{\substack{n=0,m=0 \\ n+m\neq 0}}^{\infty} \left\{ [A_{i_{n,m}}cosh\lambda_{n,m}z + B_{i_{n,m}}sinh\lambda_{n,m}z] \times \cos\left(\frac{n\pi x}{W_1}\right)\cos\left(\frac{m\pi y}{W_2}\right) \right\} \qquad (19)$$

where $\lambda_{n,m} = \sqrt{(n\pi/W_1)^2 + (m\pi/W_2)^2}$.

For each layer the constants $A_{n,m}$ and $B_{n,m}$ are to be determined.

Substituting (19) into (17) yields

$$A_{i_{0,0}} + B_{i_{0,0}}h_i + \sum_{\substack{n=0,m=0 \\ n+m\neq 0}}^{\infty} \left\{ [A_{i_{n,m}}cosh\lambda_{n,m}h_i + B_{i_{n,m}}sinh\lambda_{n,m}h_i] \times \cos\left(\frac{n\pi x}{W_1}\right)\cos\left(\frac{m\pi y}{W_2}\right) \right\} =$$

$$= A_{i+1_{0,0}} + B_{i+1_{0,0}}h_{i+1} + \sum_{\substack{n=0,m=0 \\ n+m\neq 0}}^{\infty} \left\{ [A_{i+1_{n,m}}cosh\lambda_{n,m}h_{i+1} + B_{i+1_{n,m}}sinh\lambda_{n,m}h_{i+1}] \times \cos\left(\frac{n\pi x}{W_1}\right)\cos\left(\frac{m\pi y}{W_2}\right) \right\}$$

$$(20)$$

which gives

$$\begin{cases} A_{i_{0,0}} + B_{i_{0,0}}h_i = A_{i+1_{0,0}} + B_{i+1_{0,0}}h_{i+1} \\ A_{i_{n,m}}cosh\lambda_{n,m}h_i + B_{i_{n,m}}sinh\lambda_{n,m}h_i = A_{i+1_{n,m}}cosh\lambda_{n,m}h_{i+1} + B_{i+1_{n,m}}sinh\lambda_{n,m}h_{i+1} \end{cases} \qquad (21)$$

Substituting (19) into (18) yields

$$\kappa_i B_{i_{0,0}} + \kappa_i \sum_{\substack{n=0,m=0 \\ n+m\neq 0}}^{\infty} \left\{ [A_{i_{n,m}}\lambda_{n,m}\sinh\lambda_{n,m}h_i + B_{i_{n,m}}\lambda_{n,m}\cosh\lambda_{n,m}h_i] \times \cos\left(\frac{n\pi x}{W_1}\right)\cos\left(\frac{m\pi y}{W_2}\right) \right\} =$$

$$= \kappa_{i+1} B_{i+1_{0,0}}$$

$$+ \kappa_{i+1} \sum_{\substack{n=0,m=0 \\ n+m\neq 0}}^{\infty} \left\{ [A_{i+1_{n,m}}\lambda_{n,m}\sinh\lambda_{n,m}h_{i+1} + B_{i+1_{n,m}}\lambda_{n,m}\cosh\lambda_{n,m}h_{i+1}] \times \cos\left(\frac{n\pi x}{W_1}\right)\cos\left(\frac{m\pi y}{W_2}\right) \right\}$$

$$(22)$$

which gives

$$\begin{cases} \kappa_i B_{i_{0,0}} = \kappa_{i+1} B_{i+1_{0,0}} \\ \kappa_i A_{i_{n,m}}\lambda_{n,m}\sinh\lambda_{n,m}h_i + \kappa_i B_{i_{n,m}}\lambda_{n,m}\cosh\lambda_{n,m}h_i = \kappa_{i+1}A_{i+1_{n,m}}\lambda_{n,m}\sinh\lambda_{n,m}h_{i+1} + \kappa_{i+1}B_{i+1_{n,m}}\lambda_{n,m}\cosh\lambda_{n,m}h_{i+1} \end{cases}$$

$$(23)$$

Using Fourier series for the current density on top surface at $z = h_L$ and replacing (19) into (12) leads to

$$\kappa_L B_{L_{0,0}} + \kappa_L \sum_{\substack{n=0,m=0 \\ n+m\neq 0}}^{\infty} \left\{ \left[A_{L_{n,m}}\lambda_{n,m}\sinh\lambda_{n,m}h_3 + B_{L_{n,m}}\lambda_{n,m}\cosh\lambda_{n,m}h_3 \right] \times \cos\left(\frac{n\pi x}{W_1}\right)\cos\left(\frac{m\pi y}{W_2}\right) \right\} = j^t(x,y) =$$

$$\sum_{n=0}^{\infty} \sum_{m=0}^{\infty} j_{n,m}^t \cos\left(\frac{n\pi x}{W_1}\right)\cos\left(\frac{m\pi y}{W_2}\right) \tag{24}$$

Equation (24) implies that

$$\begin{cases} \kappa_L B_{L_{0,0}} = j_{0,0}^t \\ \kappa_L A_{L_{n,m}}\lambda_{n,m}\sinh\lambda_{n,m}h_L + \kappa_L B_{L_{n,m}}\lambda_{n,m}\cosh\lambda_{n,m}h_L = j_{m,n}^t \end{cases} \tag{25}$$

Similarly, Fourier series for the current density on bottom surface at $z = h_0$ with replacing (19) into (13) leads to

$$\begin{cases} \kappa_1 B_{L_{0,0}} = j_{0,0}^b \\ \kappa_1 A_{1_{n,m}}\lambda_{n,m}\sinh\lambda_{n,m}h_1 + \kappa_1 B_{1_{n,m}}\lambda_{n,m}\cosh\lambda_{n,m}h_1 = j_{m,n}^b \end{cases} \tag{26}$$

The components of Fourier series $j_{m,n}^t$ and $j_{m,n}^b$ are known and given in [25].
It can be easily proven that equations (23) , (25), and (26) for $n = 0$ and $m = 0$ are dependent. In order to obtain 2L independent equations corresponding to $A_{n,m}$ and $B_{n,m}$, equation (16) should be used.
Substituting (19) into (16) yields

$$U_1(x,y,z) = A_{1_{0,0}} + B_{1_{0,0}}h_0 + \sum_{\substack{n=0,m=0 \\ n+m\neq 0}}^{\infty} \left\{ [A_{1_{n,m}}\cosh\lambda_{n,m}h_0 + B_{1_{n,m}}\sinh\lambda_{n,m}h_0] \times \cos\left(\frac{n\pi x}{W_1}\right)\cos\left(\frac{m\pi y}{W_2}\right) \right\} = U_0$$

$$(27)$$

In [25], this analytical problem was solved for a single layered region. The authors mentioned since $A_{0,0}$ was a ground voltage it was set to zero. Equation (24) indicates that it is true and $A_{1_{0,0}}$ not only depends on ground voltage but also is a function of the amplitudes of other Fourier series components.

To demonstrate an implementation of the proposed formulation, we consider a four-layered region. The components in equation (21), (23), (25), and (26) for $n + m \neq 0$ yield the following equations

$$\begin{bmatrix} \cosh\lambda_{n,m}h_1 & \sinh\lambda_{n,m}h_1 & -\cosh\lambda_{n,m}h_1 & -\sinh\lambda_{n,m}h_1 & 0 & 0 & 0 & 0 \\ 0 & 0 & \cosh\lambda_{n,m}h_2 & \sinh\lambda_{n,m}h_2 & -\cosh\lambda_{n,m}h_2 & -\sinh\lambda_{n,m}h_2 & 0 & 0 \\ 0 & 0 & 0 & 0 & \cosh\lambda_{n,m}h_3 & \sinh\lambda_{n,m}h_3 & -\cosh\lambda_{n,m}h_3 & -\sinh\lambda_{n,m}h_3 \\ \kappa_1\lambda_{n,m}\sinh\lambda_{n,m}h_1 & \kappa_1\lambda_{n,m}\cosh\lambda_{n,m}h_1 & -\kappa_2\lambda_{n,m}\sinh\lambda_{n,m}h_1 & -\kappa_2\lambda_{n,m}\cosh\lambda_{n,m}h_1 & 0 & 0 & 0 & 0 \\ 0 & 0 & \kappa_2\lambda_{n,m}\sinh\lambda_{n,m}h_2 & \kappa_2\lambda_{n,m}\cosh\lambda_{n,m}h_2 & -\kappa_3\lambda_{n,m}\sinh\lambda_{n,m}h_2 & -\kappa_3\lambda_{n,m}\cosh\lambda_{n,m}h_2 & 0 & 0 \\ 0 & 0 & 0 & 0 & \kappa_3\lambda_{n,m}\sinh\lambda_{n,m}h_3 & \kappa_3\lambda_{n,m}\cosh\lambda_{n,m}h_3 & -\kappa_4\lambda_{n,m}\sinh\lambda_{n,m}h_3 & -\kappa_4\lambda_{n,m}\cosh\lambda_{n,m}h_3 \\ 0 & 0 & 0 & 0 & 0 & 0 & \kappa_4\lambda_{n,m}\sinh\lambda_{n,m}h_4 & \kappa_4\lambda_{n,m}\cosh\lambda_{n,m}h_4 \\ 0 & -\kappa_1\lambda_{n,m} & 0 & 0 & 0 & 0 & 0 & 0 \end{bmatrix} \begin{bmatrix} A_{1_{n,m}} \\ B_{1_{n,m}} \\ A_{2_{n,m}} \\ B_{2_{n,m}} \\ A_{3_{n,m}} \\ B_{3_{n,m}} \\ A_{4_{n,m}} \\ B_{4_{n,m}} \end{bmatrix} = \begin{bmatrix} 0 \\ 0 \\ 0 \\ 0 \\ 0 \\ 0 \\ j_{n,m}^t \\ j_{n,m}^b \end{bmatrix}$$

After computation of $A_{n,m}$ and $B_{n,m}$ for for $n+m \neq 0$, the components for $n=0$ and $m=0$ are obtained as

$$
\begin{bmatrix}
1 & h_1 & -1 & -h_1 & 0 & 0 & 0 & 0 \\
0 & 0 & 1 & h_2 & -1 & -h_2 & 0 & 0 \\
0 & 0 & 0 & 0 & 1 & h_3 & -1 & -h_3 \\
0 & \kappa_1 & 0 & -\kappa_2 & 0 & 0 & 0 & 0 \\
0 & 0 & 0 & \kappa_2 & 0 & -\kappa_3 & 0 & 0 \\
0 & 0 & 0 & 0 & 0 & \kappa_3 & 0 & -\kappa_4 \\
0 & 0 & 0 & 0 & 0 & 0 & 0 & \gamma_4 \\
1 & z_0 & 0 & 0 & 0 & 0 & 1 & 0
\end{bmatrix}
\begin{bmatrix}
A_{1_{0,0}} \\
B_{1_{0,0}} \\
A_{2_{0,0}} \\
B_{2_{0,0}} \\
A_{3_{0,0}} \\
B_{3_{0,0}} \\
A_{4_{0,0}} \\
B_{4_{0,0}}
\end{bmatrix}
=
\begin{bmatrix}
0 \\
0 \\
0 \\
0 \\
0 \\
0 \\
j_{0,0}^t \\
U_0 - S_1
\end{bmatrix}
$$

where $S_1 = \sum_{\substack{n=0,m=0 \\ n+m \neq 0}}^{\infty} \left\{ [A_{1_{n,m}} \cosh\lambda_{n,m} z_0 + B_{1_{n,m}} \sinh\lambda_{n,m} z_0] \times \cos\left(\frac{n\pi x_0}{h_1}\right) \cos\left(\frac{m\pi y_0}{h_2}\right) \right\}$

The voltage of the l-th electrode on the top plane is given by

$$V_l^t = \frac{1}{A_{el}} \int_{e_l} U(s) ds$$

$$= A_{L_{0,0}} + B_{L_{0,0}} h_L$$

$$+ \frac{1}{A_{el}} \sum_{\substack{n=0,m=0 \\ n+m \neq 0}}^{\infty} \left\{ \left[A_{L_{n,m}} \cosh\lambda_{n,m} h_L + B_{L_{n,m}} \sinh\lambda_{n,m} h_L \right] \times \iint_{e_l} \cos\frac{n\pi x}{W_1} \cos\frac{m\pi y}{W_2} dx dy \right\}$$

Similarly, the voltage of the k-th electrode on the bottom plane is obtained as

$$V_k^b = \frac{1}{A_{ek}} \int_{e_k} U(s) ds$$

$$= A_{1_{0,0}} + B_{1_{0,0}} h_0$$

$$+ \frac{1}{A_{ek}} \sum_{\substack{n=0,m=0 \\ n+m \neq 0}}^{\infty} \left\{ \left[A_{1_{n,m}} \cosh\lambda_{n,m} h_0 + B_{1_{n,m}} \sinh\lambda_{n,m} h_0 \right] \times \iint_{e_k} \cos\frac{n\pi x}{W_1} \cos\frac{m\pi y}{W_2} dx dy \right\}$$

When the voltages of l-th electrode on the top plane and k-th electrode on the bottom plate are measured and the currents of l-th electrode and k-th electrode be I and $-I$, the impedance can be obtained as

$$Z_{lk} = \frac{V_l^t - V_k^b}{I}$$
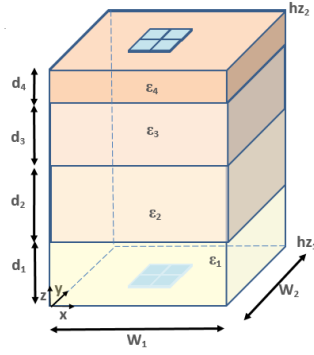
IV.   SIMULATION RESULTS

Example 1:

Fig. 6. Estimation of permitivity for a model of four-layered tissue with analytical and FE solutions
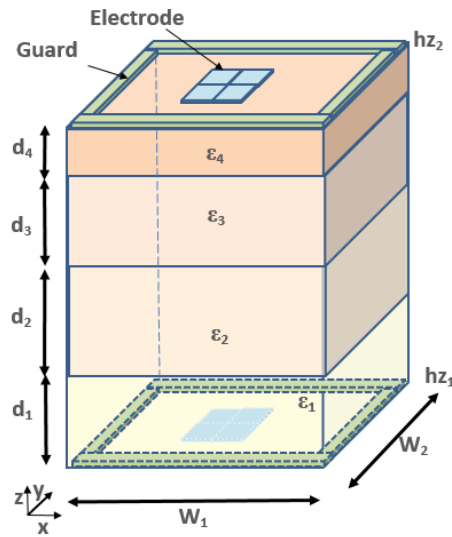
Example 2:

Fig. 7. Estimation of permitivity for a model of four-layered tissue with FE solutions

Example 3: Method Veification Results

A.   For the methods validation, ε_r of the Plexiglas was measured at 2.9±0.15 with an excitation frequency of 32 kHz. Considering linear variation approximation of EP over the frequency range of 60 Hz-100 kHz, the given ε_r range of 3.5-2.7 leads to 3.24. This value is sufficiently close to the ε_r values measured in our validation experiment. It is worth noting that the 3.24 value is only an approximate value obtained based on the linear approximation assumption over the given range of frequencies.

B.   *Tissue relative EP measurement results*

The relative permittivity values of the 35 bovine specimens, which were obtained using the proposed technique, are presented in Fig. 8. These values are 12162±1800, 11630±1403, 31550±2391 and 283±20 for the left ventricle, right ventricle, liver and trabecular bone samples, respectively.
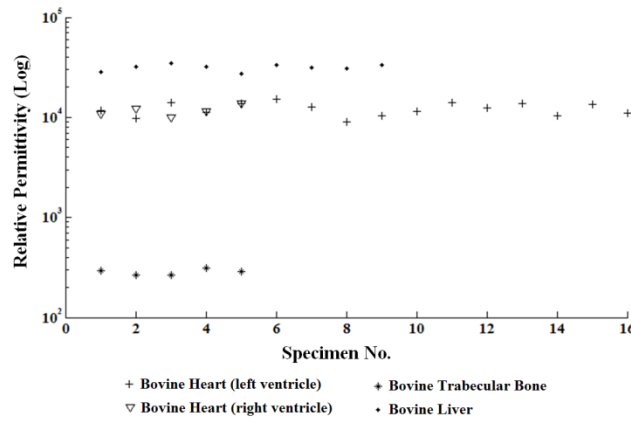
Fig. 8. ε_r values of bovine heart, liver and trabecular bone specimens at 32 kHz.

The standard deviation values pertaining to the measurements are only 14%, 12%, 7% and 7% of the corresponding average values of the left ventricle, right ventricle, liver and trabecular bone, respectively. This demonstrates relatively high repeatability of the proposed measurement method, especially that the observed permittivity variations include inter and intra specimen variability in addition to experimental errors. It is noteworthy that in Fig. 8, the left ventricle tissue specimens 11 to 16 correspond to the curved shape specimens while the rest correspond to the block shaped specimens. T-test was conducted to assess statistical differences between measured ε_r values of these two groups of specimens. The test led to p = 0.5794, indicating that the differences are not statistically significant which demonstrates insensitivity of the proposed method to specimen geometry. This consolidates that the proposed method is capable of estimating tissue ε_r accurately irrespective of the specimen's geometric complexity. Table 1 shows the ε_r values from the proposed technique for the heart, trabecular bone and liver specimens are within the reported ε_r range in the literature by previous researchers such as Gabriel et al. [7,8].

TABLE I.   COMPARISON BETWEEN BOVINE RELATIVE EP VALUES OBTAINED FROM THE PROPOSED TECHNIQUE AND CORRESPONDING VALUES REPORTED IN THE LITERATURE FOR THE SAME TYPE OF TISSUES AT 32 kHz.

Specimen's Type	Mean $\varepsilon_r \pm$ STD	Reported ε_r in the Literature
Bovine heart (LV, n=16)	12162±1800	10000 -20000 [7,8]
Bovine heart (LV, n=5)	11630±1403	
Bovine liver (n=9)	31550 ±2391	10000-30000 [7,8]
Bovine trabecular bone (n=5)	283 ± 19.5	200-300 [7,8]

Due to the accuracy of the capacitance data processing model used in the proposed technique, the ε_r values obtained in this study are expected to have improved accuracy compared to the ones reported in the literature.

C.   CONCLUSIONS

The technique presented in this article was developed for measurement of relative EP of small ex-vivo tissue specimens. It uses a capacitive sensor consisting of two parallel plates where the tissue sample is placed between the plates and acts as its dielectric. To extract this information, we developed an inverse FE algorithm which inputs the measured capacitance, sensor's configuration data including the specimen's geometry and boundary conditions, known electrical properties of sensor's plates and excitation voltage to output the tissue specimen's relative EP.
For small highly complex shaped tissue specimens acquired from surgeries, imaging using computed tomography or magnetic resonance imaging followed by image segmentation maybe required to capture their geometry and incorporate them into the FE model. The standard deviation of the measured relative EP values were at 7% to 14% of their corresponding average values. These values indicate high measurement repeatability as the corresponding variances include inter- and intra-specimen variability in addition to experimental errors. The ε_r measurement of bovine specimens in this study was performed at frequency of 32 kHz only. However, the proposed technique, can be used to measure ε_r of tissues at a wide range of frequencies. The proposed method can be used potentially for the estimation of permittivity in layered dielectric media.

REFERENCES

[1] R. J. Halter, A. Hartov, J. A. Heaney, K. D. Paulsen, and A. R. Schned, "Electrical impedance spectroscopy of the human prostate," IEEE Trans. Biomed. Eng., vol. 54, no. 7, pp. 1321-1327 , July 2007.

[2] R. J. Halter , A. Schned, J. Heaney, A. Hartov, and K. D. Paulsen, "Electrical impedance spectroscopy of benign and malignant prostatic tissues, " J. Urol., vol. 179, no. 4, pp. 1580-1586, April 2008.

[3] R. J. Halter, A. Hartov, and K. D. Paulsen, "A broadband high-frequency electrical impedance tomography system for breast imaging, " IEEE Trans. Biomed. Eng., vol. 55, no. 2, pp. 650-659, February 2008.

[4] P J Dimbylow, "Development of pregnant female, hybrid voxel-mathematical models and their application to the dosimetry of applied magnetic and electric fields at 50 Hz", Phys. Med. Biol., vol. 51, no. 10, pp.2383–2394, April 2006.

[5] P. M. Meaney, T. Zhou, D. Goodwin, A. Golnabi, E. A. Attardo, K. D. Paulsen, "Bone Dielectric Property Variation as a Function of Mineralization at Microwave Frequencies, " International Journal of Biomedical Imaging, vol. 2012, Article ID 649612, 2012.

[6] P. M. Meaney, A. P. Gregory, J. Seppälä, T. Lahtinen, "Open-Ended Coaxial Dielectric Probe Effective Penetration Depth Determination," IEEE Trans. Microwave Theory Tech., vol. 64, no. 3, pp. 915-923, March 2016.

[7] S. Gabriel, R. W. Lau, and C. Gabriel, "The dielectric properties of biological tissues: II. Measurements in the frequency range 10 Hz to 20 GHz, " Phys. Med. Biol. vol. 41, no.11, pp. 2251–2269, November 1996.

[8] S. Gabriel, R. W. Lau and C. Gabriel, "The dielectric properties of biological tissues: III. Parametric models for the dielectric spectrum of tissues, " Phys. Med. Biol., vol. 41, no. 11, pp.2271–2293, November 1996.

[9] C. Gabriel, A. Peyman, and E. H. Grant, "Electrical conductivity of tissue at frequencies below 1MHz, " Phys. Med. Biol. vol. 54, no. 16, pp. 4863–4878, July 2009.

[10] C. Gabriel and A. Peyman, "Dielectric measurement: error analysis and assessment of uncertainty, " Phys. Med. Biol., vol. 51, no. 23, pp. 6033–6046, December 2006.

[11] A Peyman, C Gabriel; Dielectric properties of porcine glands, gonads and body fluids, Phys. Med. Biol., vol. 57, no. 19, N339–N344, September 2012.

[12] A Peyman, C Gabriel; Dielectric properties of rat embryo and foetus as a function of gestation, Phys. Med. Biol., vol. 57, no. 8, pp. 2103-2116, March 2012.

[13] Y. Lu , H. Cui, J. Yu, and S. Mashimo, "Dielectric properties of human fetal organ tissues at radio frequencies, " Bioelectromagnetics, vol. 17, no. 5, pp. 425-426, 1996.

[14] W. T. Joines, Y. Zhang, C. Li, and R. L. Jirtle, "The measured electrical properties of normal and malignant human tissues from 50 to 900 MHz, " Med. Phys., vol. 21, no. 4, pp. 547-550, April 1994.

[15] J. B. Jarvis, M. D. Janezic, P. D. Domich, and R. G. Geyer "Analysis of an open-ended coaxial probe with lift-off for nondestructive testing, " IEEE Trans. Instrum. Meas., vol. 43, no. 5, pp. 711-718, October 1994.

[16] J. B. Jarvis et al., "Measuring the permittivity and permeability of lossy materials: solids, liquids, metals, building materials, and negative-index materials, " NIST, Washington, Tech. Note 1536, February 2005.

[17] M.S. Venkatesh and G.S.V. Raghavan, "An overview of dielectric properties measuring techniques, " Canadian Biosystems Engineering, vol. 47, no. 17, pp. 15-30, 2005.

[18] J. M. Jin, The Finite Element Method in Electromagnetics, 3rd ed., Hoboken, NJ: John Wiley & Sons, 2002, pp. 168–175.

[19] C. Gabriel, T. Y. A. Chan, and E. H. Grant, "Admittance models for open ended coaxial probes and their place in dielectric spectroscopy, " Phys. Med. Biol., vol. 39, no. 12, pp. 2138-2200, December 1994

[20] S. M. Hesabgar, A. Sadeghi-Naini , G. Czarnota, and A. Samani, "Dielectric properties of the normal and malignant breast tissues in xenograft mice at low frequencies (100 Hz–1 MHz), " Measurement, vol. 105, pp. 56–65, July 2017.

[21] E. Haber, U. M. Ascher, and D. Oldenburg, "On optimization techniques for solving nonlinear inverse problems, " Inverse Problems, vol. 16, no. 5, pp. 1263–1280, 2000.

[22] J. G. Webster, ed., Electrical Measurement, Signal Processing, and Displays, New York, CRC Press, 2004, pp. 10-3.

[23] J. G. Webster, Medical Instrumentation: Application and Design, John Wiley & Sons, Inc., 1995.

[24] S. M. Hesabgar, R. Jafari, and A, Samani, "Accurate Technique for Measuring Electrical Permittivity of Biological Tissues at Low Frequencies and Sensitivity Analysis," in IEEE Int. Symp. MeMeA, Rome, Italy, 2018.

[25] M. H. Choi, T. Kao, D. Isaacson, G. J. Saulnier, and J. C. Newell, "A Reconstruction Algorithm for Breast Cancer Imaging With Electrical Impedance Tomography in Mammography Geometry," IEEE Transactions On Biomedical Engineering, vol. 54, no. 4, April 2007.

[26] R. Kulkarni, G. Boverman, D. Isaacson, G. J Saulnier, T. Kao and J. C Newell,"An analytical layered forward model for breasts in electrical impedance tomography, " Physiol. Meas. 29, S27–S40, 2008.

[27] R. Kulkarni, T. Kao, G. Boverman, D. Isaacson, G. J Saulnier and J. C Newell, "A two-layered forward model of tissue for electrical impedance tomography," Physiol. Meas. 30, S19–S34, 2009.

[28] R. Kulkarni, G. Boverman, D. Isaacson, G. Saulnier, and J. C. Newell, "Layered Model for Breasts in Electrical Impedance Tomography", Proceedings of the 29th Annual International Conference of the IEEE EMBS, Cité Internationale, Lyon, France, August 23-26, 2007.

[29] Rujuta Kulkarni, "Analytical Forward Models For Breast Cancer Detection Using Electrical Impedance Tomography," Ph.D. dissertation, Rensselaer Polytechnic Institute,Troy, New York, 2009.